

Cavity-Free Distributed Quantum Computing with Rydberg Ensembles via Collective Enhancement

Aman Ullah^{1,*}

¹*Department of Physics, University of Nevada, Reno, NV 89557, USA*

A complete architecture for cavity-free quantum networking based on collective enhancement in Rydberg atom ensembles is presented. The protocol exploits Rydberg blockade and phase-matched directional emission to eliminate optical cavities without sacrificing performance. The architecture comprises three steps: (i) local control-ensemble entanglement via Rydberg blockade with fidelity $F_{\text{gate}} \approx 99.93\%$; (ii) atom-photon conversion via Raman transitions, achieving directional emission ($\eta_{\text{dir}} \approx 35\%$) and single-node efficiency $\eta_{\text{node}} \approx 19\%$; and (iii) remote atom-atom entanglement via Hong-Ou-Mandel interference, producing Bell states with fidelity $F > 97.5\%$. With quantum memories enabling retry protocols, entanglement generation rates exceed 600 Hz at 20 km separation. This cavity-free approach provides a practical and scalable pathway for distributed quantum computing and secure quantum communication.

Quantum networks distribute entanglement between distant nodes, enabling secure communication, and distributed quantum computing [1–6]. Significant progress, both experimental and theoretical, toward realizing such networks has been achieved across different physical platforms, including trapped ions [7–10], nitrogen-vacancy centers in diamond [11–13], and neutral atoms [14–16]. Among these, neutral atoms are particularly attractive due to their long coherence times, strong and controllable Rydberg-mediated interactions, and natural compatibility with photonic interfaces [17–20].

The Rydberg blockade mechanism—where a single Rydberg excitation suppresses additional excitations within a blockade radius via strong van der Waals interactions—provides a powerful tool for quantum information processing. This effect has enabled high-fidelity two-qubit gates [21–25], multi-particle entangled states [26–28], and programmable quantum simulators [29, 30]. Within the same Rydberg framework, entanglement between a control atom and an ensemble of N atoms has been explored as a resource for quantum networking, leveraging the ensemble’s collective enhancement for efficient light-matter interfaces [31–35]. Separately, atom-photon coupling and heralded photonic entanglement have been demonstrated in cavity-based systems [36, 37]. Cavities, while effective, impose narrow bandwidths and introduce experimental complexity that hinders scalability. However, despite progress in these individual components, a unified cavity-free protocol that integrates deterministic local entanglement, efficient photon generation, and heralded remote entanglement into a complete quantum network architecture remains unrealized.

In this Letter, a comprehensive three-step protocol (Fig. 1) is presented that establishes a complete cavity-free quantum network architecture. **Step 1** (local entanglement) exploits Rydberg blockade and collective coupling enhancement to generate high-fidelity entanglement $|\psi_1\rangle$ between a control atom and an ensemble of $N \approx 1000$ atoms. The control atom is prepared in a superposition of ground and Rydberg states, while strong van der Waals interactions confine the ensemble to a single collective Rydberg excitation shared across all

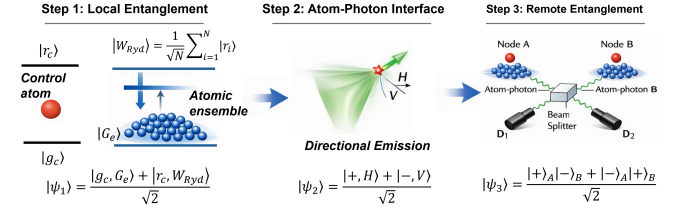


FIG. 1: Three-step protocol for cavity-free quantum networking with Rydberg atoms. **Step 1:** A control atom (red) and atomic ensemble are entangled via Rydberg blockade. Energy levels show the control atom states $|g_c\rangle$ (ground) and $|r_c\rangle$ (Rydberg), and ensemble states $|G_e\rangle$ (collective ground state) and $|W_{\text{Ryd}}\rangle$ (collective Rydberg excitation), generating the entangled state $|\psi_1\rangle$. **Step 2:** Raman transitions map the collective excitation to a directional photon (green cone). State-selective coupling to Rydberg magnetic sublevels encodes quantum information in photon polarizations $|H\rangle$ and $|V\rangle$, creating the atom-photon state $|\psi_2\rangle$. **Step 3:** Constructive interference at a beam splitter with heralding detectors (D_1 , D_2) generates the remote Bell state $|\psi_3\rangle$.

atoms. This collective excitation yields an enhanced effective Rabi frequency $\Omega_{\text{eff}} = \sqrt{N}\Omega$, where Ω is the single-atom Rabi frequency, enabling fast control while Rydberg blockade restricts dynamics to the single-excitation manifold [38, 39]. **Step 2** (atom-photon interface) converts the local entanglement into atom-photon entanglement $|\psi_2\rangle$ via Raman transitions that map the collective excitation onto a propagating photon. A spatial phase gradient imprinted across the ensemble ensures phase-matched emission, producing a directional photon efficiently coupled into an optical fiber. The Raman process simultaneously provides state-selective coupling between Rydberg magnetic sublevels and photon polarizations, generating a photonic qubit entangled with the control atom and encoded in polarization states $|H\rangle$ and $|V\rangle$. This combination of directional emission and polarization encoding enables high collection efficiency suitable for subsequent remote entanglement attempts. **Step 3** combines photons from two independent nodes at a beam splitter, where Hong-Ou-Mandel interference [40] and heralded single-photon detection [41] generate the remote Bell state $|\psi_3\rangle$.

Step 1: Local Entanglement.—Rydberg blockade generates deterministic local entanglement between a control atom and a collective Rydberg excitation in an atomic ensemble (Fig. 1,

* aullah@unr.edu

Step 1). The system comprises a control atom with states $|g_c\rangle$ (ground) and $|r_c\rangle$ (Rydberg), and an ensemble of $N \approx 1000$ atoms, each with ground $|g\rangle$ and Rydberg $|r\rangle$ states. The ensemble is initially prepared in the collective ground state $|G_e\rangle = \bigotimes_{i=1}^N |g_i\rangle$.

Rydberg atoms interact via the van der Waals potential $V(r) = C_6/r^6$, where C_6 is the van der Waals coefficient. For interaction strengths exceeding the single-atom Rabi frequency Ω within a blockade radius $r_b = (C_6/\hbar\Omega)^{1/6}$, states with multiple Rydberg excitations are energetically suppressed. This Rydberg blockade confines the ensemble to the single-excitation subspace spanned by $|G_e\rangle$ and the singly-excited states $|r_i\rangle \equiv |g_1 \cdots r_i \cdots g_N\rangle$. The symmetric superposition $|W_{\text{Ryd}}\rangle = N^{-1/2} \sum_{i=1}^N |r_i\rangle$ couples to $|G_e\rangle$ with collectively enhanced Rabi frequency $\Omega_{\text{eff}} = \sqrt{N}\Omega$, reducing the ensemble to an effective two-level system.

The four relevant basis states are $|g_c, G_e\rangle, |g_c, W_{\text{Ryd}}\rangle, |r_c, G_e\rangle, |r_c, W_{\text{Ryd}}\rangle$, with dynamics governed by the Hamiltonian

$$H = H_c + \frac{\hbar\Omega_{\text{eff}}}{2} (|W_{\text{Ryd}}\rangle \langle G_e| + \text{h.c.}) + V |r_c, W_{\text{Ryd}}\rangle \langle r_c, W_{\text{Ryd}}|, \quad (1)$$

where $H_c = \frac{\hbar\Omega}{2} (|r_c\rangle \langle g_c| + \text{h.c.})$ drives the control atom, the second term drives the collectively enhanced ensemble transition, and V denotes the van der Waals interaction between the control atom and ensemble. For $V \gg \Omega_{\text{eff}}$, the doubly-excited state $|r_c, W_{\text{Ryd}}\rangle$ is energetically inaccessible, confining dynamics to the three-state manifold $|g_c, G_e\rangle, |r_c, G_e\rangle, |g_c, W_{\text{Ryd}}\rangle$ (see Supplemental Material (SM) Sec. S1).

Entanglement is generated via a two-pulse protocol, illustrated in Fig. 2(a), starting from $|g_c, G_e\rangle$: (i) a $\pi/2$ pulse on the control atom (duration $t_{\pi/2} = \pi/(2\Omega)$) creates the superposition $|\psi_c\rangle = (|g_c, G_e\rangle + |r_c, G_e\rangle)/\sqrt{2}$; (ii) a subsequent π pulse on the ensemble (duration $t_\pi = \pi/\Omega_{\text{eff}} = \pi/(\sqrt{N}\Omega)$) conditionally drives $|G_e\rangle \leftrightarrow |W_{\text{Ryd}}\rangle$. The blockade prevents this transition when the control atom is in $|r_c\rangle$, since $|r_c, W_{\text{Ryd}}\rangle$ is off-resonant by V . This conditional evolution,

$$|g_c, G_e\rangle \xrightarrow{\pi\text{-pulse}} -i |g_c, W_{\text{Ryd}}\rangle, \quad |r_c, G_e\rangle \xrightarrow{\pi\text{-pulse}} |r_c, G_e\rangle, \quad (2)$$

yields the maximally entangled Bell state

$$|\psi_1\rangle = \frac{1}{\sqrt{2}} (|r_c, G_e\rangle - i |g_c, W_{\text{Ryd}}\rangle), \quad (3)$$

correlating the control atom state with the collective ensemble excitation.

Numerical simulation (Fig. 2(a)) confirms Bell state generation with fidelity $F = 99.93\%$ for $N = 1000$ atoms and blockade strength $V/\Omega_{\text{eff}} = 15.8$. Collective enhancement enables fast operation: for $\Omega/2\pi = 10$ MHz, $\Omega_{\text{eff}}/2\pi \approx 316$ MHz and $t_\pi \approx 1.6$ ns. This Bell state serves as the input for Step 2, where $|W_{\text{Ryd}}\rangle$ is mapped onto a photonic qubit.

Step 2: Atom-Photon Interface.—Constructing the photonic interface for remote quantum communication (Fig. 1, Step 2) requires three capabilities: (i) mapping the collective Rydberg excitation $|W_{\text{Ryd}}\rangle$ to an optical transition with high fidelity, (ii) emitting the photon directionally for efficient fiber

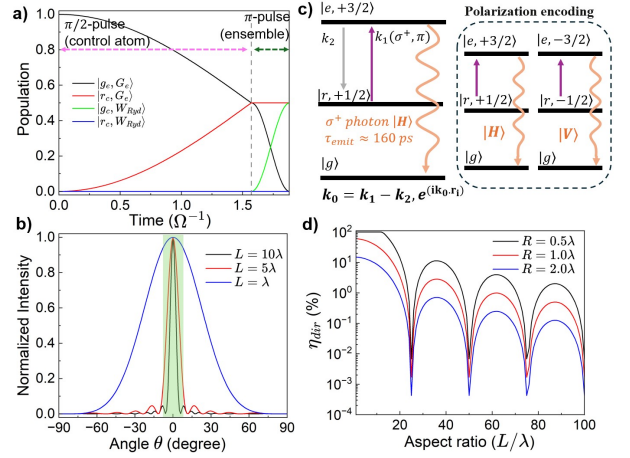


FIG. 2: **Protocol performance and mechanisms.** (a) Step 1 dynamics: $\pi/2$ pulse on control atom (left dashed line) followed by conditional π pulse on ensemble (right dashed line) generates Bell state $|\psi_1\rangle$. Blockade suppresses $|r_c, W_{\text{Ryd}}\rangle$ (blue, $< 10^{-4}$). (b) Step 2 Raman mapping: Collective Rydberg state $|W_{\text{Ryd}}\rangle$ is transferred to optical collective state with phase $e^{ik_0 \cdot r_i}$ for directional emission. State-selective coupling to magnetic sublevels $|r, \pm 1/2\rangle$ yields polarization-encoded photons $|H\rangle, |V\rangle$ (inset). (c) Angular emission pattern for $L/\lambda = 10$ (black), 5 (red), 1 (blue). Elongated clouds ($L = 10\lambda$) give narrow cone ($\Delta\theta \approx 5.7^\circ$) matching fiber acceptance (green, $\pm 6^\circ$). (d) Directional efficiency η_{dir} vs L/λ for $R/\lambda = 0.5$ (black), 1.0 (red), 2.0 (blue). Operating point ($L = 10\lambda, R = \lambda$, red dot) yields $\eta_{\text{dir}} \approx 0.35$.

coupling, and (iii) encoding quantum information in a photonic degree of freedom.

The conversion begins by mapping $|W_{\text{Ryd}}\rangle = N^{-1/2} \sum_i |r_i\rangle$ to an optically excited collective state $|W_e\rangle$ via a two-photon Raman transition. This mapping imprints spatially varying phases $e^{ik_0 \cdot r_i}$ that enable directional emission:

$$|W_e\rangle = \frac{1}{\sqrt{N}} \sum_{i=1}^N e^{ik_0 \cdot r_i} |e_i\rangle, \quad (4)$$

where $|e_i\rangle$ represents the optically excited state (e.g., $5P_{3/2}$ in ^{87}Rb), and \mathbf{k}_0 is the desired emission wavevector determined by the Raman beam geometry. These phases ensure constructive interference along $\hat{\mathbf{k}}_0$ and destructive interference elsewhere, concentrating emission into a narrow cone. Crucially, this collective optical state couples to the electromagnetic field with \sqrt{N} enhancement: the interaction Hamiltonian

$$H_{\text{int}} = \hbar g \sqrt{N} (\hat{a}_{\mathbf{k}_0}^\dagger |G_e\rangle \langle W_e| + \text{h.c.}), \quad (5)$$

yields a collective spontaneous emission rate $\Gamma_{\text{coll}} = N\Gamma_0$, where Γ_0 is the single-atom decay rate [42–44]. For $N = 1000$ atoms and $\Gamma_0/2\pi \approx 6$ MHz, this gives an emission time $\tau_{\text{emit}} \sim 160$ ps—dramatically faster than single-atom decay and sufficient to suppress decoherence during mapping.

The directionality is quantified by the array factor $F(\theta) = N^{-1} \sum_i e^{i(\mathbf{k}-\mathbf{k}_0) \cdot \mathbf{r}_i}$, where \mathbf{k} is the emitted photon wavevector at angle θ from $\hat{\mathbf{k}}_0$, and $|\mathbf{k}| = k_0 = 2\pi/\lambda$ with λ the photon wavelength. For a cigar-shaped cloud of length L and radius R aligned along \mathbf{k}_0 , the atom number N cancels with

density, making the angular pattern depend only on geometry. In the limit $R \ll L$, one obtains $F(\theta) = \text{sinc}(k_0 L \sin \theta/2)$ (SM Sec. S2), giving an intensity distribution $|F(\theta)|^2$ with angular half-width $\Delta\theta \approx \lambda/L$. Figure 2(b) shows this pattern for different aspect ratios: elongated clouds with $L = 10\lambda$ (black curve) produce a narrow emission cone ($\Delta\theta \approx 5.7^\circ$) well-matched to typical fiber numerical apertures (NA ~ 0.1 , acceptance $\pm 6^\circ$, green shaded region), while spherical geometries with $L = \lambda$ (blue curve) yield nearly isotropic emission.

The directional efficiency—the fraction of photons emitted into the fiber acceptance angle θ_{\max} ,

$$\eta_{\text{dir}} = \frac{\int_0^{\theta_{\max}} |F(\theta)|^2 \sin \theta d\theta}{\int_0^{\pi/2} |F(\theta)|^2 \sin \theta d\theta}, \quad (6)$$

depends critically on both L and R . Figure 2(d) shows η_{dir} versus aspect ratio L/λ for different transverse radii. Smaller R (black curve, $R = 0.5\lambda$) yields higher peak efficiencies due to tighter transverse confinement, while oscillations at large L arise from side lobes outside the fiber acceptance. For our optimized geometry $L = 10\lambda$, $R = \lambda$ (red curve), full numerical integration yields $\eta_{\text{dir}} \approx 0.35$ —a $35\times$ enhancement over isotropic free-space emission, comparable to low-finesse cavities but without their fabrication complexity (SM Sec. S3).

Atom-photon entanglement requires encoding quantum information in a degree of freedom robust against fiber decoherence. Polarization encoding is employed (Fig. 2(c)), where the logical basis $|0\rangle_L, |1\rangle_L$ maps to horizontal and vertical polarizations $|H\rangle, |V\rangle$. This is achieved through polarization-selective Raman coupling: orthogonal beam polarizations address different magnetic sublevels of the Rydberg state,

$$\begin{aligned} |r, m_j = +\frac{1}{2}\rangle &\xrightarrow{\sigma^+, \pi} |e, m'_j = +\frac{3}{2}\rangle \longrightarrow |g\rangle + |H\rangle, \\ |r, m_j = -\frac{1}{2}\rangle &\xrightarrow{\sigma^-, \pi} |e, m'_j = -\frac{3}{2}\rangle \longrightarrow |g\rangle + |V\rangle, \end{aligned} \quad (7)$$

where m_j denotes angular momentum projection. The effective Raman Hamiltonian,

$$H_{\text{Raman}} = \frac{\hbar\Omega_R}{2} \sum_{i=1}^N e^{ik_0 \cdot \mathbf{r}_i} (|e_i, m'_j\rangle \langle r_i, m_j| + \text{h.c.}), \quad (8)$$

maps each Rydberg sublevel to the corresponding optical excited state with the phase factor required for directional emission. Spontaneous emission from these states, governed by angular momentum selection rules, produces circularly polarized photons: $|e, +\frac{3}{2}\rangle$ decays to $|g, +\frac{1}{2}\rangle$ emitting σ^+ , while $|e, -\frac{3}{2}\rangle$ decays to $|g, -\frac{1}{2}\rangle$ emitting σ^- . A quarter-wave plate converts these to linear polarizations $|H\rangle$ and $|V\rangle$. For emission within $\Delta\theta < 10^\circ$ of $\hat{\mathbf{k}}_0$, polarization purity exceeds 95% (SM Sec. S4).

Combining these elements, the full transformation from the

Step 1 Bell state proceeds as:

$$\begin{aligned} |\psi_1\rangle &= \frac{1}{\sqrt{2}} (|r_c, G_e\rangle - i |g_c, W_{\text{Ryd}}\rangle) |0\rangle \\ &\xrightarrow{H_{\text{Raman}}} \frac{1}{\sqrt{2}} (|r_c, G_e\rangle |0\rangle - i |g_c, W_e\rangle |0\rangle) \\ &\xrightarrow{H_{\text{emission}}} \frac{1}{\sqrt{2}} (|r_c, G_e\rangle |0\rangle - i |g_c, G_e\rangle |H\rangle_{\mathbf{k}_0}), \end{aligned} \quad (9)$$

where we have taken the control atom to be in the $m_j = +1/2$ sublevel for simplicity. For a control atom prepared in an equal superposition of both Rydberg sublevels (achieved by appropriate initialization in Step 1), polarization-resolved detection yields the entangled state

$$|\psi_2\rangle = \frac{1}{\sqrt{2}} (|r_c, +\frac{1}{2}\rangle |G_e\rangle |H\rangle + |r_c, -\frac{1}{2}\rangle |G_e\rangle |V\rangle), \quad (10)$$

where the control atom's spin state is now entangled with the photon polarization—exactly the resource needed for subsequent remote entanglement protocols.

The overall single-node efficiency combines three factors:

$$\eta_{\text{node}} = F_{\text{gate}} \times \eta_{\text{dir}} \times \eta_{\text{map}}, \quad (11)$$

with $F_{\text{gate}} \approx 0.99$ (Step 1 fidelity), $\eta_{\text{dir}} \approx 0.35$ (directional collection), and $\eta_{\text{map}} \approx 0.55$ (Raman transfer and spontaneous emission losses, including off-axis emission, imperfect polarization purity, and finite optical depth). For $N = 1000$, $\eta_{\text{node}} \approx 0.19$ —the probability that a successful Step 1 gate produces a high-fidelity atom-photon entangled state with the photon emitted into the fiber mode. This modest value necessitates quantum memory for retry attempts; we implement this via electromagnetically induced transparency (EIT) [45, 46], storing the photonic qubit as a collective spin wave with retrieval efficiency $\eta_r \approx 0.55$ and coherence time $T_2 > 100 \mu\text{s}$ (SM Sec. S5). This memory enables the protocol to repeatedly attempt remote entanglement generation without destroying the initial control-ensemble entanglement from Step 1—a crucial capability given the low success probability per attempt ($P_E \approx 0.56\%$, as shown in Step 3).

Having established the photonic interface, each node generates atom-photon entangled states $|\psi_2\rangle$ with efficiency $\eta_{\text{node}} \approx 0.19$. In Step 3, two such nodes are combined to generate remote atom-atom entanglement through photonic interference and heralded detection.

Step 3: Remote Entanglement via Photonic Interference.—The photons emitted from two nodes are directed to a central station where they interfere on a beamsplitter. Coincidence detection of orthogonal polarizations heralds a maximally entangled state between the remote atoms (Fig. 1, Step 3).

For two identical nodes A and B , each in the state from Step 2, control atoms in Rydberg sublevels $|+\rangle \equiv |r, m_j = +\frac{1}{2}\rangle$ and $|-\rangle \equiv |r, m_j = -\frac{1}{2}\rangle$ are entangled with horizontally ($|H\rangle$) and vertically ($|V\rangle$) polarized photons, respectively. Assuming the photons from both nodes are indistinguishable in frequency, temporal mode, and spatial mode (achieved through laser stabilization and temporal synchronization via quantum

memories), the joint initial state is

$$|\Psi_{AB}\rangle = \frac{1}{2} \left(|+\rangle_A |+\rangle_B |H\rangle_A |H\rangle_B + |+\rangle_A |-\rangle_B |H\rangle_A |V\rangle_B \right. \\ \left. + |-\rangle_A |+\rangle_B |V\rangle_A |H\rangle_B + |-\rangle_A |-\rangle_B |V\rangle_A |V\rangle_B \right). \quad (12)$$

The photons combine on a 50:50 non-polarizing beam-splitter. Hong-Ou-Mandel interference causes photons with identical polarization ($|H\rangle_A |H\rangle_B$ or $|V\rangle_A |V\rangle_B$) to bunch together, yielding zero coincidence probability. Only cross-polarized inputs ($|H\rangle_A |V\rangle_B$ or $|V\rangle_A |H\rangle_B$) contribute to coincidence events. Applying the beamsplitter transformation and projecting onto outcomes with one photon in each output mode and orthogonal polarizations (detailed derivation in SM Sec. S6) yields the heralded atomic states

$$|\psi_{H_c, V_d}\rangle = \frac{1}{\sqrt{2}} (-|+\rangle_A |-\rangle_B + |-\rangle_A |+\rangle_B), \quad (13)$$

$$|\psi_{V_c, H_d}\rangle = \frac{1}{\sqrt{2}} (|+\rangle_A |-\rangle_B - |-\rangle_A |+\rangle_B), \quad (14)$$

which are maximally entangled Bell states. Thus, coincidence detection of orthogonal polarizations projects the remote atoms onto entanglement.

The ideal heralding probability is $P_{\text{herald}} = 1/4$, with each coincidence pattern occurring with probability $1/8$. In practice, node efficiencies η_{node} , propagation losses η_{prop} , and detection efficiency η_{det} reduce the success probability per attempt to

$$P_E = \frac{1}{4} \eta_{\text{node}}^2 \eta_{\text{prop}}^2 \eta_{\text{det}}^2. \quad (15)$$

For $\eta_{\text{node}} \approx 0.19$, $\eta_{\text{prop}} \approx 0.8$ (short distances), and $\eta_{\text{det}} \approx 0.8$, this yields $P_E \approx 0.37\%$. At metropolitan-scale separations (~ 20 km), fiber attenuation ($\alpha \approx 0.2$ dB/km at telecom wavelengths) reduces η_{prop} to approximately 0.4, giving $P_E \approx 0.09\%$ (SM Sec. S7).

Fidelity of the heralded entanglement depends on photon indistinguishability. Any mismatch in frequency, temporal mode, or spatial mode reduces the two-photon interference visibility V , degrading fidelity as $F = (1 + V)/2$. With careful laser stabilization, temporal synchronization, and mode matching in single-mode fibers, visibilities $V > 0.95$ are achievable, yielding fidelities $F > 97.5\%$.

The modest P_E values necessitate quantum memory to enable retry attempts. Each node incorporates the EIT-based memory from Step 2 with retrieval efficiency $\eta_r \approx 0.55$ and coherence time $T_2 > 100 \mu\text{s}$. After an unsuccessful attempt, the atom-photon entangled state can be regenerated via Step 2 within the control atom's coherence time. The cumulative success probability after M attempts is $P_{\text{cumulative}} = 1 - (1 - P_E)^M$. Figure 3(a) shows this enhancement: for our parameters ($P_E \approx 0.5\%$, red curve), $M = 100$ attempts yield $\sim 40\%$ cumulative success probability. With regeneration time $T_{\text{regen}} \sim 1 \mu\text{s}$ per attempt, such retry protocols are feasible within the memory coherence time.

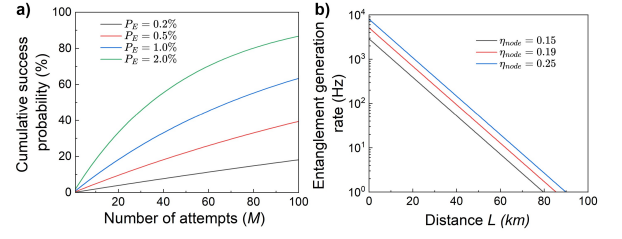


FIG. 3: **Remote entanglement performance.** (a) Cumulative success probability versus attempts M for $P_E = 0.2\%$ (black), 0.5% (red), 1.0% (blue), and 2.0% (green). Quantum memory enables $M \sim 100$ attempts within T_2 , yielding $\sim 40\%$ cumulative probability for $P_E = 0.5\%$. (b) Entanglement rate R versus distance for node efficiencies $\eta_{\text{node}} = 0.15$ (black), 0.19 (red), and 0.25 (blue). For $\eta_{\text{node}} = 0.19$, R exceeds 600 Hz at 20 km, enabling metropolitan-scale applications.

The entanglement generation rate is $R = P_E/T_{\text{cycle}}$, where T_{cycle} includes state regeneration, photon propagation, and detection latency. Figure 3(b) shows the distance dependence for different node efficiencies, accounting for exponential fiber attenuation. For our parameters ($\eta_{\text{node}} = 0.19$, red curve) and $T_{\text{cycle}} \approx 1 \mu\text{s}$, the protocol achieves rates exceeding 600 Hz at 20 km separation—sufficient for distributed quantum computing applications. Higher node efficiencies ($\eta_{\text{node}} = 0.25$, blue curve) enable rates exceeding 1 kHz at metropolitan scales, demonstrating clear pathways for performance optimization (for detail see SM Secs. S8-S11).

Discussion.—This work presents a complete three-step protocol for cavity-free quantum networking using Rydberg atom ensembles. The protocol achieves: (i) local control-ensemble entanglement with fidelity $F_{\text{gate}} \approx 99.93\%$ via Rydberg blockade (Fig. 2a), (ii) atom-photon conversion with single-node efficiency $\eta_{\text{node}} \approx 19\%$ through directional emission (Fig. 2b-d), and (iii) remote atom-atom entanglement with fidelity $F > 97.5\%$ and generation rates exceeding 600 Hz at 20 km separation (Fig. 3). This cavity-free architecture provides a practical foundation for metropolitan-scale quantum networks without sacrificing the high fidelities required for distributed quantum computing and secure communication.

The protocol's key advantage is the elimination of optical cavities through collective enhancement. Step 1 exploits Rydberg blockade to create a decoherence-free subspace where N atoms collectively couple with strength $\Omega_{\text{eff}} = \sqrt{N}\Omega$, enabling fast gates ($t_\pi \sim 1.6$ ns) that suppress spontaneous emission losses. Step 2 uses phase-matched Raman transitions to achieve directional emission ($\eta_{\text{dir}} \approx 35\%$) comparable to low-finesse cavities but without fabrication complexity or mode-matching constraints. The combination yields $\eta_{\text{node}} \approx 19\%$, sufficient for practical quantum networking when combined with quantum memories.

Several pathways exist for performance optimization. Increasing N to 10^4 atoms (achievable in optical dipole traps) would enhance η_{dir} through tighter spatial confinement while maintaining fast gates via stronger blockade. Optimizing cloud geometry and Raman beam alignment could improve η_{map} beyond 70% . Advanced EIT techniques (e.g., ladder

schemes, optimized pulse shapes) could increase memory efficiency η_r toward 80%, directly boosting η_{node} . These improvements would increase P_E by factors of 2–5, enabling kilohertz-scale entanglement rates at metropolitan distances.

The protocol is compatible with existing Rydberg platforms [16, 24, 39]. The required laser systems (780 nm for optical transitions, 480 nm for Rydberg excitation) are commercially available. Detection efficiencies $\eta_{\text{det}} > 95\%$ are achievable with superconducting nanowire detectors [47]. Recent demonstrations of atom-photon entanglement over 20 km [48] and atom-atom entanglement over 33 km [49] in deployed fiber networks confirm the feasibility of the proposed 20 km operational range. Thus, near-term experimental realization is feasible with current technology.

Conclusion.—A complete cavity-free architecture for quantum networking based on Rydberg atom ensembles has been presented. By exploiting collective enhancement in both entanglement generation and photon emission, the protocol achieves performance metrics suitable for distributed quantum computing: gate fidelities $> 99\%$, Bell state fidelities $> 97.5\%$, and entanglement generation rates exceeding 600 Hz at 20 km separation. The elimination of optical cavities significantly reduces experimental complexity while maintaining competitive performance, providing a practical pathway toward scalable metropolitan-scale quantum networks. Future work will focus on experimental demonstration and extension to multi-node network topologies.

-
- [1] A. K. Ekert, *Physical Review Letters* **67**, 661 (1991).
- [2] J. I. Cirac, A. K. Ekert, S. F. Huelga, and C. Macchiavello, *Physical Review A* **59**, 4249 (1999).
- [3] C. L. Degen, F. Reinhard, and P. Cappellaro, *Reviews of Modern Physics* **89**, 035002 (2017).
- [4] H. J. Kimble, *Nature* **453**, 1023 (2008).
- [5] S. Wehner, D. Elkouss, and R. Hanson, *Science* **362**, eaam9288 (2018).
- [6] C. M. Knaut, A. Suleymanzade, Y.-C. Wei, D. R. Assumpcao, P.-J. Stas, Y. Q. Huan, B. Machielse, E. N. Knall, M. Sutula, G. Baranes, *et al.*, *Nature* **629**, 573 (2024).
- [7] C. D. Bruzewicz, J. Chiaverini, R. McConnell, and J. M. Sage, *Applied physics reviews* **6** (2019).
- [8] R. Blatt and C. F. Roos, *Nature Physics* **8**, 277 (2012).
- [9] P. Drmota, D. Main, D. P. Nadlinger, B. C. Nichol, M. A. Weber, E. M. Ainley, A. Agrawal, R. Srinivas, G. Araneda, C. J. Ballance, *et al.*, *Physical Review Letters* **130**, 090803 (2023).
- [10] M. Pompili, S. L. Hermans, S. Baier, H. K. Beukers, P. C. Humphreys, R. N. Schouten, R. F. Vermeulen, M. J. Tiggeleman, L. dos Santos Martins, B. Dirkse, *et al.*, *Science* **372**, 259 (2021).
- [11] K. Nemoto, M. Trupke, S. J. Devitt, A. M. Stephens, B. Scharfenberger, K. Buczak, T. Nöbauer, M. S. Everitt, J. Schmiedmayer, and W. J. Munro, *Physical Review X* **4**, 031022 (2014).
- [12] N. Y. Yao, L. Jiang, A. V. Gorshkov, P. C. Maurer, G. Giedke, J. I. Cirac, and M. D. Lukin, *Nature communications* **3**, 800 (2012).
- [13] P. C. Maurer, G. Kucsko, C. Latta, L. Jiang, N. Y. Yao, S. D. Bennett, F. Pastawski, D. Hunger, N. Chisholm, M. Markham, *et al.*, *Science* **336**, 1283 (2012).
- [14] M. Saffman, *National Science Review* **6**, 24 (2019).
- [15] L. Henriot, L. Beguin, A. Signoles, T. Lahaye, A. Browaeys, G.-O. Reymond, and C. Jurczak, *Quantum* **4**, 327 (2020).
- [16] J. P. Covey, H. Weinfurter, and H. Bernien, *npj Quantum Information* **9**, 90 (2023).
- [17] T. Xia, M. Lichtman, K. Maller, A. W. Carr, M. J. Piotrowicz, L. Isenhower, and M. Saffman, *Physical Review Letters* **114**, 100503 (2015).
- [18] Y. Wang, A. Kumar, T.-Y. Wu, and D. S. Weiss, *Science* **352**, 1562 (2016).
- [19] Y. O. Dudin, L. Li, and A. Kuzmich, *Physical Review A* **87**, 031801 (2013).
- [20] W. Xu, A. V. Venkatramani, S. H. Cantú, T. Šumarac, V. Klüsener, M. D. Lukin, and V. Vuletić, *Physical Review Letters* **127**, 050501 (2021).
- [21] S. J. Evered, D. Bluvstein, M. Kalinowski, S. Ebadi, T. Manovitz, H. Zhou, S. H. Li, A. A. Geim, T. T. Wang, N. Maskara, *et al.*, *Nature* **622**, 268 (2023).
- [22] S. Ma, G. Liu, P. Peng, B. Zhang, S. Jandura, J. Claes, A. P. Burgers, G. Pupillo, S. Puri, and J. D. Thompson, *Nature* **622**, 279 (2023).
- [23] L. Isenhower, E. Urban, X. Zhang, A. Gill, T. Henage, T. A. Johnson, T. Walker, and M. Saffman, *Physical review letters* **104**, 010503 (2010).
- [24] H. Levine, A. Keesling, G. Semeghini, A. Omran, T. T. Wang, S. Ebadi, H. Bernien, M. Greiner, V. Vuletić, H. Pichler, and M. D. Lukin, *Physical Review Letters* **123**, 170503 (2019).
- [25] T. M. Graham, M. Kwon, B. Grinkemeyer, Z. Marra, X. Jiang, M. T. Lichtman, Y. Sun, M. Ebert, and M. Saffman, *Physical Review Letters* **123**, 230501 (2019).
- [26] T. Wilk, A. Gaëtan, C. Evellin, J. Wolters, Y. Miroshnychenko, P. Grangier, and A. Browaeys, *Physical review letters* **104**, 010502 (2010).
- [27] J. Zeiher, R. Van Bijnen, P. Schauß, S. Hild, J.-y. Choi, T. Pohl, I. Bloch, and C. Gross, *Nature Physics* **12**, 1095 (2016).
- [28] D. Bluvstein, S. J. Evered, A. A. Geim, S. H. Li, H. Zhou, T. Manovitz, S. Ebadi, M. Cain, M. Kalinowski, D. Hangleiter, *et al.*, *Nature* **626**, 58 (2024).
- [29] H. Bernien, S. Schwartz, A. Keesling, H. Levine, A. Omran, H. Pichler, S. Choi, A. S. Zibrov, M. Endres, M. Greiner, V. Vuletić, and M. D. Lukin, *Nature* **551**, 579 (2017).
- [30] P. Scholl, M. Schuler, H. J. Williams, A. A. Eberharter, D. Barredo, K.-N. Schymik, V. Lienhard, L.-P. Henry, T. C. Lang, T. Lahaye, A. M. Läuchli, and A. Browaeys, *Nature* **595**, 233 (2021).
- [31] M. Saffman and T. Walker, *Physical Review A—Atomic, Molecular, and Optical Physics* **72**, 042302 (2005).
- [32] Y. Dudin and A. Kuzmich, *Science* **336**, 887 (2012).
- [33] Y. Dudin, L. Li, F. Bariani, and A. Kuzmich, *Nature Physics* **8**, 790 (2012).
- [34] T. Weber, M. Hönig, T. Niederprüm, T. Manthey, O. Thomas, V. Guarrera, M. Fleischhauer, G. Barontini, and H. Ott, *Nature Physics* **11**, 157 (2015).
- [35] N. L. Spong, Y. Jiao, O. D. Hughes, K. J. Weatherill, I. Lesanovsky, and C. S. Adams, *Physical Review Letters* **127**, 063604 (2021).
- [36] J. D. Thompson, T. G. Tiecke, N. P. de Leon, J. Feist, A. V. Akimov, M. Gullans, A. S. Zibrov, V. Vuletić, and M. D. Lukin,

- Science **340**, 1202 (2013).
- [37] E. Togan, Y. Chu, A. S. Trifonov, L. Jiang, J. Maze, L. Childress, M. V. G. Dutt, A. S. Sørensen, P. R. Hemmer, A. S. Zibrov, and M. D. Lukin, *Nature* **466**, 730 (2010).
- [38] M. Ebert, M. Kwon, T. G. Walker, and M. Saffman, *Physical Review Letters* **112**, 043602 (2014).
- [39] M. Saffman, T. G. Walker, and K. Mølmer, *Reviews of modern physics* **82**, 2313 (2010).
- [40] C.-K. Hong, Z.-Y. Ou, and L. Mandel, *Physical review letters* **59**, 2044 (1987).
- [41] L.-M. Duan, M. D. Lukin, J. I. Cirac, and P. Zoller, *Nature* **414**, 413 (2001).
- [42] M. Gross and S. Haroche, *Physics reports* **93**, 301 (1982).
- [43] R. H. Dicke, *Physical review* **93**, 99 (1954).
- [44] S. J. Masson, I. Ferrier-Barbut, L. A. Orozco, A. Browaeys, and A. Asenjo-Garcia, *Physical review letters* **125**, 263601 (2020).
- [45] S. E. Harris, *Physics today* **50**, 36 (1997).
- [46] M. Fleischhauer and M. D. Lukin, *Physical review letters* **84**, 5094 (2000).
- [47] F. Marsili, V. B. Verma, J. A. Stern, S. Harrington, A. E. Lita, T. Gerrits, I. Vayshenker, B. Baek, M. D. Shaw, R. P. Mirin, *et al.*, *Nature Photonics* **7**, 210 (2013).
- [48] T. van Leent, M. Bock, R. Garthoff, K. Redeker, W. Zhang, T. Bauer, W. Rosenfeld, C. Becher, and H. Weinfurter, *Physical review letters* **124**, 010510 (2020).
- [49] T. Van Leent, M. Bock, F. Fertig, R. Garthoff, S. Eppelt, Y. Zhou, P. Malik, M. Seubert, T. Bauer, W. Rosenfeld, *et al.*, *Nature* **607**, 69 (2022).